Accelerated light carbon sequestration following late Paleocene-early Eocene carbon cycle perturbations

Victor A. Piedrahita [a,*], Xiang Zhao [a], Andrew P. Roberts [a], Eelco J. Rohling [a,b],
David Heslop [a], Simone Galeotti [c,d], Laura Rodríguez-Sanz [a], Fabio Florindo [d,e],
Katharine M. Grant [a]

[a] Research School of Earth Sciences, Australian National University, ACT 2601, Canberra, Australia
[b] School of Ocean and Earth Science, University of Southampton, National Oceanography Centre, SO14 3ZH, Southampton, UK
[c] Dipartimento di Scienze Pure e Applicate, Università degli Studi di Urbino, 61029, Urbino, Italy
[d] Institute for Climate Change Solutions, Via Sorchio 61040, Frontone, Pesaro e Urbino, Italy
[e] Istituto Nazionale di Geofisica e Vulcanologia, Via di Vigna Murata 605, 00143, Rome, Italy

ARTICLE INFO

ABSTRACT

Carbon releases into the climate system produce global warming and ocean acidification events that can be reversed eventually by carbon sequestration. However, the underlying controls on the timescales of carbon removal, and their dependence on the amplitude of the initial perturbation, are poorly understood. Here, we assess a series of late Paleocene-early Eocene (LPEE) carbon cycle perturbations (∼56-52 Ma) of different amplitudes to constrain carbon removal timescales. Carbon isotope excursions (CIEs) and sedimentation patterns for the largest event, the Paleocene-Eocene Thermal Maximum (PETM), allow identification of a light carbon injection that appeared ∼85 kyr after the PETM onset. This CIE may have been triggered by orbital forcing of long (∼400 kyr) and short (∼100 kyr) eccentricity maxima. The various LPEE light carbon injections were followed by exponential carbon removal trends with half-life ($t_{1/2}$) estimates of ∼6-26 kyr. These values are smaller than background estimates for the modern carbon cycle ($t_{1/2} > 100$ kyr), which reveals accelerated light carbon sequestration. We find that one estimated $t_{1/2}$ period coincided temporally with ocean acidification recovery in different locations with contrasting paleo-water depths. This pattern indicates enhanced chemical weathering following LPEE CIEs; however, chemical weathering timescales are an order of magnitude longer than the observed $t_{1/2}$ estimates. This reveals that several carbon processes were optimized during LPEE CIE recovery. Similar $t_{1/2}$ estimates are obtained for light carbon injections of different sizes, which suggests that carbon removal was optimized to conditions induced by the initial perturbation. Temperature controls on oxygen solubility may have accelerated the oceanic biological pump in proportion to each LPEE carbon injection. This process may have caused accelerated carbon sequestration during LPEE CIE recovery and produced the short carbon removal timescales identified by $t_{1/2}$ estimates of LPEE carbon cycle perturbations.

1. Introduction

Future social and economic impacts of anthropogenic CO_2 emissions are partially identified through shared socio-economic pathways (SSPs). SSPs are related to possible greenhouse gas concentration scenarios that define upcoming climate conditions (Meinshausen et al., 2020). SSP 8.5 is associated with a fourfold atmospheric CO_2 concentration increase to ∼1500 ppm in the next ∼100-300 years, which may dramatically strengthen global warming and ocean acidification (Rae et al., 2021). Adverse impacts of a SSP 8.5-like carbon concentration scenario can be eventually reversed by carbon sequestration; however, carbon sequestration timescales, and time constraints for negative environmental impacts, remain elusive for SSP 8.5-like carbon cycle perturbations. Late Paleocene-early Eocene (LPEE; ∼56-52 Ma) sedimentary archives contain records of a series of light carbon injections that produced global warming/ocean acidification events with different magnitudes (Cramer et al., 2003). These events can be compared to a future SSP 8.5-like global warming state in terms of temperature and atmospheric CO_2 concentrations (Burke et al., 2018; Westerhold et al., 2020; Rae et al., 2021). Hence, LPEE carbon cycle perturbations offer opportunities to gauge poorly known carbon

* Corresponding author.
E-mail address: victor.piedrahitavelez@anu.edu.au (V.A. Piedrahita).

sequestration timescales and may be useful for identifying relationships between emission amplitudes, carbon removal, and ocean acidification recovery.

LPEE climates were characterized by a long-term trend of increasing temperature that was punctuated by short-lived ($\leq$200 kyr-long) carbon cycle perturbations. These events include hyperthermals such as the Paleocene-Eocene Thermal Maximum (PETM, $\sim$56 Ma), the Eocene Thermal Maximum (ETM) 2 ($\sim$54 Ma), and ETM 3 ($\sim$52.8 Ma), and other smaller carbon cycle perturbations that are labelled with letters (Cramer et al., 2003). LPEE carbon cycle perturbations have been identified close to both orbital long ($\sim$400 kyr) and short eccentricity ($\sim$100 kyr) maxima (Lourens et al., 2005; Galeotti et al., 2010; Zeebe and Lourens, 2019; Piedrahita et al., 2022). This orbital configuration produced insolation and temperature changes that, under long-term global warming, destabilized biospheric carbon stocks and/or methane hydrates, which caused massive carbon releases to the ocean-atmosphere and triggered LPEE short-lived carbon cycle perturbations (Lunt et al., 2011; DeConto et al., 2012). In contrast to other early Eocene carbon cycle perturbations, the PETM, which was the largest LPEE carbon cycle perturbation, has been interpreted to be associated with several carbon releases from diverse reservoirs. Orbitally controlled thermal destabilization of carbon reservoirs was likely accompanied by carbon emission from the North Atlantic Igneous Province (NAIP) at the PETM onset, which may have contributed to the large magnitude of this event (Gutjahr et al., 2017; Kender et al., 2021).

LPEE carbon cycle perturbations are identified in stable carbon isotope ($\delta^{13}C$) records by negative carbon isotope excursions (CIEs) and can be divided into single or paired events (Galeotti et al., 2010; Zachos et al., 2010; Littler et al., 2014; Lauretano et al., 2018). Paired CIEs–i.e., ETM 2 and H2, and the I1 and I2 events–reflect two separate orbitally controlled carbon injections (Cramer et al., 2003; Barnet et al., 2019). These CIE events are generally associated with orbitally paced $CaCO_3$ dissolution horizons that coincide with ascending flanks of short eccentricity cycles, which reveals lysocline shoaling related to ocean acidification (Galeotti et al., 2010; Zachos et al., 2010). $CaCO_3$ dissolution horizons of paired CIEs are separated by $CaCO_3$-rich layers that were deposited during short eccentricity minima, and indicate lysocline deepening (Galeotti et al., 2010; Zachos et al., 2010). In contrast to early Eocene records, PETM sections commonly contain exceptionally long ($\geq$120 kyr) lysocline shoaling conditions and sustained low $\delta^{13}C$ values that have not been recognized to similar extents in other LPEE carbon cycle perturbations (van der Meulen et al., 2020; Zeebe and Lourens, 2019). These PETM features have been interpreted to result from ongoing light carbon injections following the event onset (Bowen, 2013; Zeebe, 2013; Frieling et al., 2016). PETM secondary light carbon releases have been suggested to be produced by NAIP activity and/or thermal destabilization of biospheric carbon stocks and/or methane hydrates (Zeebe et al., 2009; Bowen, 2013; Frieling et al., 2016). However, it is unknown if carbon releases following the PETM onset had any relationship with the same orbitally controlled driving mechanisms that have been hypothesized to trigger succeeding early Eocene carbon cycle perturbations (Lourens et al., 2005; Lunt et al., 2011; DeConto et al., 2012).

LPEE light carbon releases are interpreted to have been followed by recovery periods in which carbon sequestration mechanisms reestablished the Earth-surface carbon cycle (ocean/ atmosphere/ biosphere) to pre-event-like conditions (Bowen and Zachos, 2010; Yasukawa et al., 2017; Tanaka et al., 2022). Carbon removal timescales, and their relationship with the magnitude of the initial carbon cycle perturbation, are poorly understood for most LPEE carbon cycle perturbations. PETM carbon sequestration timescales have been assessed using exponential decay functions in $\delta^{13}C$ records, which are defined through a gradual transition from light to heavy $\delta^{13}C$ values after PETM light carbon injections (e.g., Bowen and Zachos, 2010). Half-life ($t_{1/2}$) estimates of these processes explain the rate at which a carbon mass in the Earth-surface carbon cycle is removed through carbonate and organic carbon burial (Bowen and Zachos, 2010); therefore, $t_{1/2}$ estimates are interpreted to depend directly on the total carbon mass in the Earth-surface carbon cycle, and to be inversely proportional to carbon flux rates to the lithosphere (carbonate and organic carbon burial). PETM $t_{1/2}$ values for Ocean Drilling Program (ODP) Site 690 ($t_{1/2} = 16.7$) from the Southern Ocean and for North American terrestrial sediments from the Polecat Bench section ($t_{1/2} = 13.9$) are an order of magnitude smaller than background estimates for the modern carbon cycle ($t_{1/2} \geq 100$ kyr; Bowen and Zachos, 2010). These estimates have been interpreted to reveal either different carbon masses and chemical weathering rates between the PETM and the modern carbon cycle, and/or notably accelerated light carbon removal during the PETM CIE recovery (Bowen and Zachos, 2010; Komar and Zeebe, 2017).

Proxy data and numerical approaches have been used to suggest that the carbon mass of the Paleogene Earth-surface carbon cycle may have been smaller than that of the modern carbon cycle (Bowen and Zachos, 2010). Furthermore, chemical weathering feedbacks may have been accelerated due to exceptionally high PETM temperatures (Pogge von Strandmann et al., 2021). Reduced carbon masses and higher carbon flux rates associated with chemical weathering may explain the relatively small $t_{1/2}$ estimates of the PETM recovery (Bowen and Zachos, 2010). Alternatively, modelling results have been used to indicate that small CIE recovery $t_{1/2}$ estimates reveal massive drawdown of PETM light carbon through organic carbon sequestration (Bowen and Zachos, 2010; Komar and Zeebe, 2017). Development of new carbon stocks and/or refueling of pre-existing terrestrial carbon reservoirs after PETM light carbon injections have been argued to have induced a transient period of accelerated organic carbon sequestration (Bowen and Zachos, 2010); however, observational evidence for this carbon sequestration mechanism is scarce. In contrast, proxy data and other modelling results suggest that rapid carbon uptake during the PETM recovery depended on an optimized oceanic biological pump, shifts in the style of calcification of $CaCO_3$ organisms, and/or marine tephra diagenesis (Ma et al., 2014; Komar and Zeebe, 2017; Boudreau et al., 2018; Kitch et al., 2021; Longman et al., 2021).

Carbon sequestration mechanisms following early Eocene carbon cycle perturbations have been interpreted to depend on marine productivity feedbacks and chemical weathering (Ma et al., 2014; Yasukawa et al., 2017). However, the underlying controls of these processes and their associated timescales remain poorly identified for early Eocene carbon cycle perturbations. Here, we constrain carbon sequestration timescales of LPEE carbon cycle perturbations using new probabilistic-based astrochronological age models and statistical assessments for a new high resolution $\delta^{13}C$ record from the Contessa Road section, Italy ($\sim$1,000-1,500 m paleo-water depth; Giusberti et al., 2009) and for available $\delta^{13}C$ data from ODP Site 1262, South Atlantic Ocean (Fig. 1a; $\sim$3600 m paleo-water depth; Zachos et al., 2005; Westerhold et al., 2007). We also study PETM recovery timescales and compare them to carbon removal timescales of other LPEE CIE events, to clarify the origins of the small PETM $t_{1/2}$ estimates. Furthermore, we assess temporal patterns of LPEE light carbon injections and ocean acidification recovery using new $CaCO_3$ data from Contessa Road and a pre-existing ODP Site 1262 Fe record. The contrasting paleo-water depths and paleogeographic positions of Contessa Road and ODP Site 1262 ensure that our numerical carbon removal estimates do not depend on a single local process. Sedimentation and lysocline depth variations of these different locations also provide a wider
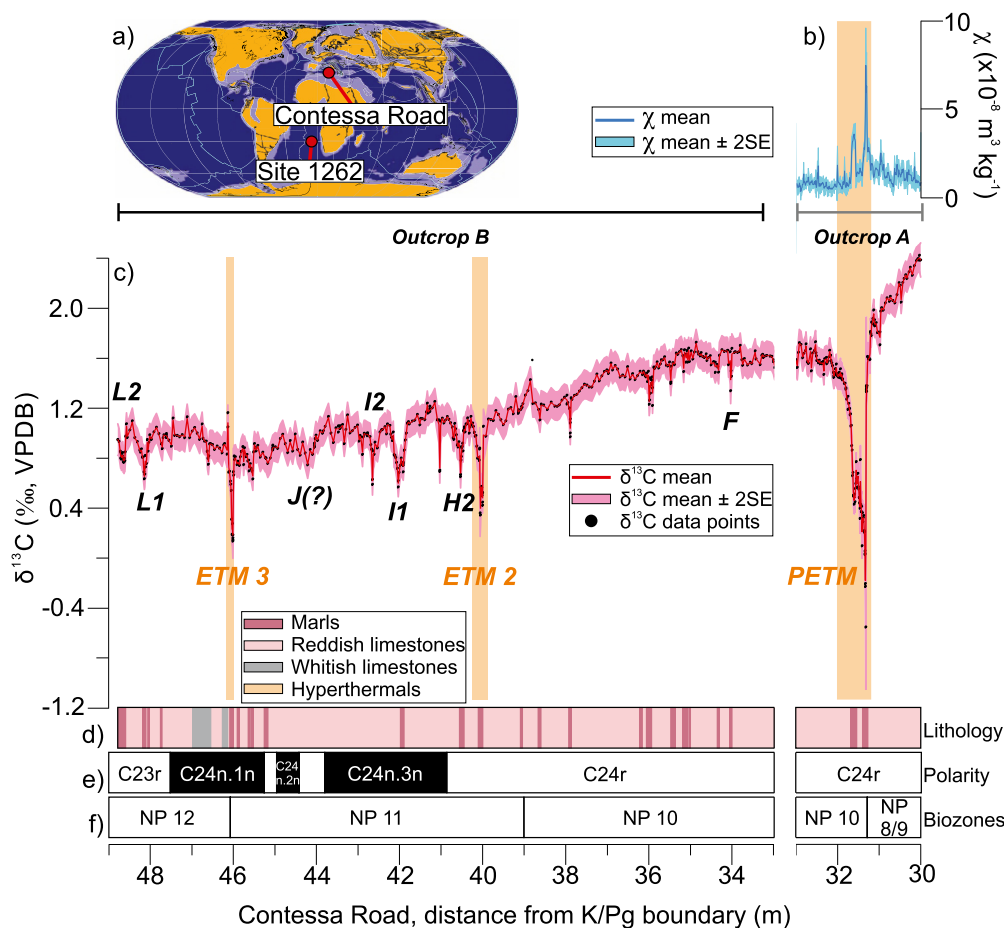
Fig. 1. (a) Paleogeographic reconstruction at ~56 Ma (Pogge von Strandmann et al., 2021) with locations of Contessa Road and ODP Site 1262. (b) χ record of Contessa Road outcrop A. (c) Contessa Road δ^{13}C record. Schematic stratigraphic summary of the studied outcrops at Contessa Road with (d) lithology, (e) magnetostratigraphy (black/white = normal/reversal polarity), and (f) biostratigraphy (calcareous nannofossil zones; Giusberti et al., 2009; Galeotti et al., 2010). χ and δ^{13}C records are presented in terms of the mean and 2SE. Orange bands represent hyperthermals. Smaller CIEs are also indicated.

perspective on the relationships between light carbon injections, carbon sequestration and ocean acidification recovery.

2. Materials and methods

2.1. Contessa road section

The Cretaceous-Paleogene Contessa Road section has records of LPEE carbon cycle perturbations in limestones and marls of the Scaglia Rossa Formation (Giusberti et al., 2009; Galeotti et al., 2010). This unit contains well-developed $CaCO_3$ dissolution cycles that have been identified by decreased $CaCO_3$ contents that correlate well with increased magnetic susceptibility (χ) values (Francescone et al., 2019). Foraminiferal assemblages and magnetic mineral variations across Contessa Road reveal that this section was affected by $CaCO_3$ dissolution, and that $CaCO_3$ dilution related to terrigenous material inputs was either minimal or did not affect sedimentation patterns of LPEE carbon cycle perturbations (Giusberti et al., 2009; Coccioni et al., 2019). Age constraints allow identification of two outcrops that contain LPEE carbon cycle perturbation records (Fig. 1b-f; *see Supplementary information*). So-called outcrop A contains PETM records in the 30-33 m depth interval at Contessa Road. Other early Eocene CIEs are contained in outcrop B, which spans the 33-48.8 m depth interval at Contessa Road (Giusberti et al., 2009; Galeotti et al., 2010). Although stratigraphic depths indicate that outcrops A and B are continuous, it is unknown if there are stratigraphic gaps between the two outcrops (*see Supplementary information*); therefore, we studied the

outcrops independently. LPEE carbon cycle perturbations at outcrops A and B are associated with marly layers (Galeotti et al., 2010) that indicate the PETM, ETM 2 and ETM 3 hyperthermals at depths of ~31.30 m, ~40 m and ~46 m, respectively (Giusberti et al., 2009; Galeotti et al., 2010). The PETM interval is characterized by two marly layers separated by a limestone layer, which is a similar sedimentation pattern to that of the ETM 2 and H2 events. In contrast, ETM 3 is identified by a single marly layer (Fig. 1d-f; *see Supplementary information*).

2.2. Sampling and laboratory analyses

Outcrop A was sampled at 1-cm resolution and outcrop B was sampled in continuous ~2-cm stratigraphic intervals, with 1-cm sample resolution across hyperthermals. Samples were used for X-ray fluorescence (XRF), χ, δ^{13}C, and wt.% $CaCO_3$ measurements (*see Supplementary information*). High-resolution $CaCO_3$ records for Contessa Road are already available (e.g., Galeotti et al., 2010); however, we did not use those data to avoid depth mismatches between our records and those of Galeotti et al. (2010). χ, XRF, and δ^{13}C measurements were carried out at the Australian National University, and wt.% $CaCO_3$ experiments were performed on the same samples at the Università degli Studi di Urbino.

2.3. Age model

Previous Contessa Road chronologies have been developed using precession-based and orbital tuning-based astrochronological

age models (Galeotti et al., 2010; Piedrahita et al., 2022). To avoid age mismatches between our new records and those of previous studies, we carried out new spectral analyses and generated probabilistic-based age models that provide ages with errors, a new feature with respect to older Contessa Road chronologies. For age model development of outcrop A, we used our new χ record to identify orbitally controlled $CaCO_3$ dissolution cycles. Orbitally controlled dissolution cycles have been recognized at Contessa Road and interpreted to indicate lysocline depth fluctuations (Galeotti et al., 2010; Francescone et al., 2019; Piedrahita et al., 2022; *see Supplementary information*). Alternatively, for age model development of outcrop B, we use our new $\delta^{13}C$ record to assess orbitally controlled carbon cycle variations. Orbital forcing of the early Eocene carbon cycle has been indicated for several early Eocene records worldwide (i.e., Westerhold et al., 2007; Zachos et al., 2010; Littler et al., 2014; Barnet et al., 2019). However, these conditions have not been recognized clearly across the PETM interval (i.e., Westerhold et al., 2007; Zachos et al., 2010); therefore, age model development using $\delta^{13}C$ records is limited to outcrop B.

Probabilistic assessments to produce Contessa Road age models were made using a Monte Carlo approach (*see Supplementary information*). Individual data points were sampled randomly within depth and experimental uncertainties. Monte Carlo iterations were then interpolated to fixed depth points and tuned to the ZB18a astronomical solution (Zeebe and Lourens, 2019) to generate empirical distributions from which mean ages with respective standard errors (SEs) were estimated (*see Supplementary information*). This protocol produces probabilistic-based astrochronological age models that were used to transfer Contessa Road $\delta^{13}C$ and wt.% $CaCO_3$ records from depth to time domains (*see Supplementary information*).

2.4. Exponential decay functions

Exponential decay functions were used to fit CIE recovery intervals of multiple LPEE carbon cycle perturbations. This method has been interpreted to provide carbon sequestration timescales following light carbon injections (Bowen and Zachos, 2010). Age and experimental errors (*see Supplementary information*) were used to develop a probabilistic approach that generates 10,000 fits across tuned $\delta^{13}C$ records from Contessa Road and ODP Site 1262. Empirical distributions were produced at each age, and the median (50th percentile) and 95% confidence interval (2.5[th] to 97.5[th] percentile) were estimated to have probabilistic-based $\delta^{13}C$ recovery fits (*see Supplementary information*).

3. Results

3.1. Orbital signals of Contessa road records

Spectral analysis (*see Supplementary information*) allows recognition of orbitally controlled periodicities in the Contessa Road records. Spectral component durations were assigned using average sedimentation rates from the Contessa Road outcrops (*see Supplementary information*). A spectral peak at ~2.79 cycles m^{-1} in the χ power spectrum can be associated with short eccentricity using the average sedimentation rate (~0.4 cm kyr^{-1}) of outcrop A (Fig. 2a). A Gaussian bandpass filter with a bandwidth of 2.79 ± 1.0 (1σ) cycles m^{-1} was used to isolate this signal. The average sedimentation rate for outcrop A indicates that this filter has a range between ~65 and ~140 kyr, which would include all short eccentricity components. Outcrop A contains sedimentation rate variations due to $CaCO_3$ dissolution across the PETM marly horizons (Piedrahita et al., 2022). PETM marly horizons indicate two lysocline shoaling events with lysocline depths above ~1,000-1,500 m. Lysocline shoaling at Contessa Road was punctuated by

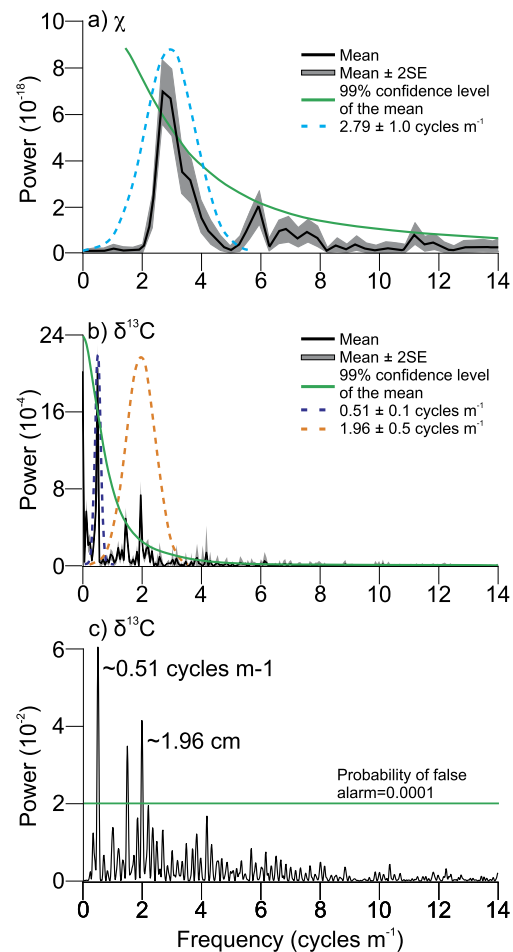**Fig. 2.** Contessa Road probabilistic power spectra of (a) χ and (b) $\delta^{13}C$. (c) Lomb-Scargle power spectrum of non-interpolated $\delta^{13}C$ data. Dashed lines in (a) and (b) represent Gaussian bandpass filters used for our age models. The 99% confidence level is indicated by green lines in (a) and (b). The green line in (c) indicates the probability of false alarm (P_{fa}) = 0.0001. Power spectra of (a) and (b) are presented in terms of the mean and 2SE.

a lysocline deepening period that is represented by a PETM limestone layer (Fig. 1b-f). This pattern confirms that Contessa Road was less affected by PETM $CaCO_3$ dissolution than other deep-ocean sites (Piedrahita et al., 2022), which is also indicated by model results that reveal less pronounced PETM lysocline shoaling in the western Tethyan Ocean compared to other regions-i.e., the South Atlantic Ocean (Zeebe et al., 2009). To avoid a filtering selection that depends exclusively on marl-limestone variations, we performed additional filter selection assessments across Contessa Road outcrop A (*see Supplementary information*).

The probabilistic-based $\delta^{13}C$ power spectrum for outcrop B has spectral peaks at ~0.51 cycles m^{-1} and ~1.96 cycles m^{-1} (Fig. 2b). According to the average sedimentation rate of outcrop B (~0.47 cm kyr^{-1}; *see Supplementary information*), these peaks can be associated with long and short eccentricity, respectively. Spectral peaks at these frequencies are also recognized in the $\delta^{13}C$ Lomb-Scargle spectrum for non-interpolated $\delta^{13}C$ data (Fig. 2c; *see Supplementary information*). This reveals that $\delta^{13}C$ periodicity is indicated by our original measurement resolution, which validates the reliability of our probabilistic-based power spectrum.

Gaussian bandpass filters with bandwidths of 0.51 ± 0.1 cycles m^{-1} and 1.96 ± 0.5 cycles m^{-1} were used to isolate short and long eccentricity components of the $\delta^{13}C$ record. Considering the average sedimentation rate at Contessa Road outcrop B, these filters have a ~350-518 kyr range for long eccentricity, and a ~86-
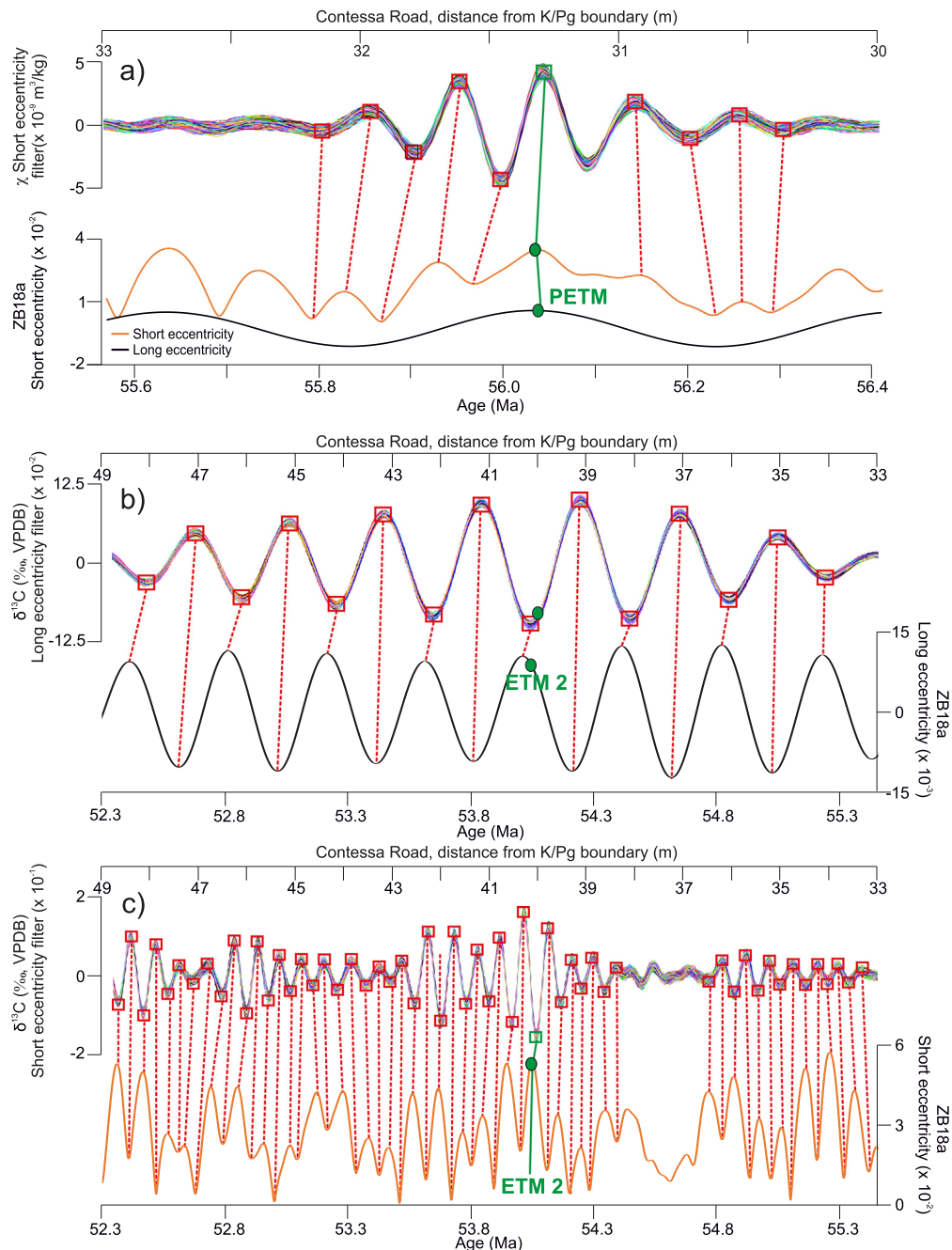
Fig. 3. Monte Carlo simulations of the filtered (a) χ short eccentricity signal, (b) δ^{13}C long eccentricity signal, and (c) δ^{13}C short eccentricity signal for Contessa Road. All records were tuned to the ZB18a orbital solution (Zeebe and Lourens, 2019). Schematic peak-trough detection windows and dashed red lines indicate tuning points. Short and long eccentricity signals of the ZB18a orbital solution (Zeebe and Lourens, 2019) are represented by orange and black lines, respectively. Green dots: PETM and ETM 2.

146 kyr range for short eccentricity. These wide intervals ensure that all components of these orbital frequencies are included in our filters. We do not discuss filter selection further for outcrop B because early Eocene orbital signals in δ^{13}C records are relatively homogeneous among sections (Zachos et al., 2010; Littler et al., 2014; Zeebe et al., 2017).

3.2. Orbital tuning of Contessa road records

Our new high-resolution δ^{13}C record allows recognition of CIEs associated with LPEE carbon cycle perturbations. We identify the PETM, ETM 2, and ETM 3 events at the same depths as indicated by previous magnetostratigraphic and biostratigraphic age constraints (Fig. 1b-d; Galeotti et al., 2010). We recognize CIEs such as H2,

I1, I2, L1 and L2, which were not identified in a low-resolution δ^{13}C record from Contessa Road ($\sim$14 cm measurement resolution; Galeotti et al., 2010). LPEE CIEs are used as age tie points for tuning of χ and δ^{13}C orbital signals. The PETM onset coincides with an abrupt χ increase at $\sim$31.30 m (Fig. 1b-c). This event was used as the main tie point for the short eccentricity signal identified in the outcrop A χ record. Only 5 short eccentricity cycles in the χ record follow the same amplitude patterns as the ZB18a astronomical solution (Fig. 3a; Zeebe and Lourens, 2019). These cycles appear between 30.36 m and 32.33 m depths, which restricts our χ-based age model to the age interval between $\sim$56.3 Ma and $\sim$55.8 Ma.

Based on biostratigraphic and magnetostratigraphic data, CIEs at $\sim$40 m and $\sim$46 m correspond to the ETM 2 and ETM 3 events,
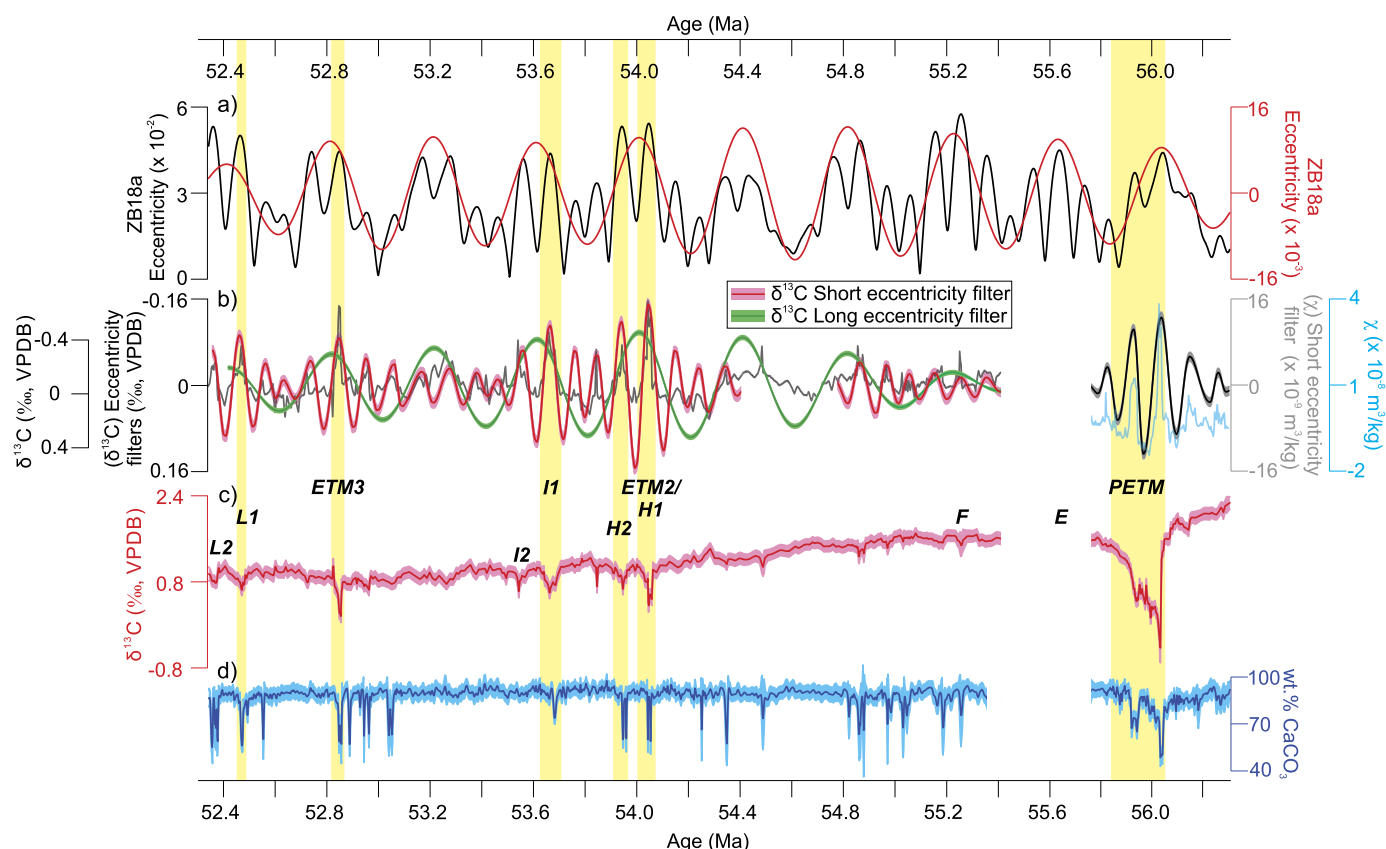
Fig. 4. (a) Short eccentricity (black) and long eccentricity (red) signals from the ZB18a orbital solution (Zeebe and Lourens, 2019). (b) Contessa Road tuned short eccentricity signals of χ (grey tones) and δ^{13}C (red tones). Contessa Road tuned long eccentricity signal of δ^{13}C is also indicated (green tones). Detrended records of mean χ and δ^{13}C are presented in blue and grey, respectively. Tuned Contessa Road (c) δ^{13}C and (d) $CaCO_3$ records. Hyperthermals (PETM, ETM 2, and ETM 3) and studied CIE events (H2, I1, and L1) are indicated by yellow bands. Smaller CIE events are labelled with letters (Lourens et al., 2005; Galeotti et al., 2010; Zachos et al., 2010). All records with probabilistic assessments are presented in terms of mean and 2SE.

respectively (Fig. 1c). This interpretation agrees with previous astrochronological age models from Contessa Road (e.g., Galeotti et al., 2010). Long and short eccentricity signals of the outcrop B δ^{13}C record were tuned independently to the ZB18a astronomical solution (Fig. 3b-c; Zeebe and Lourens, 2019). Importantly, LPEE δ^{13}C orbital signals have been interpreted to follow contrasting patterns with respect to astronomical solutions. These indicate that long and short eccentricity minima in δ^{13}C records coincide with long and short eccentricity maxima in astronomical solutions (Zachos et al., 2010; Littler et al., 2014; Zeebe et al., 2017). We followed this interpretation to tune δ^{13}C orbital signals from Contessa Road outcrop B (*see Discussion*).

Long eccentricity signals in the δ^{13}C record have well developed cycles that can be tuned to the long eccentricity signal of the ZB18a astronomical solution (Fig. 3b; Zeebe and Lourens, 2019). Short eccentricity cycles also modulate in accordance with the ZB18a orbital solution (Zeebe and Lourens, 2019) and were used for age model construction (Fig. 3c). The 54.4-54.8 Ma interval lacks well-developed short eccentricity cycles. During this age interval, the ZB18a astronomical solution (Zeebe and Lourens, 2019) also has poorly-developed short eccentricity cycles with unclear peaks compared to the rest of the astronomical solution, which hinders tuning of our short eccentricity signals (Fig. 3c). Therefore, our age model for that ~400 kyr period was developed using long eccentricity δ^{13}C cycles (Fig. 3b). This interval does not contain CIEs that are of interest here for paleoenvironmental interpretations.

Orbital tuning of Contessa Road records to the ZB18a astronomical solution (Zeebe and Lourens, 2019) indicates that all recog-

nized LPEE carbon cycle perturbations correlate with long eccentricity maxima (Fig. 4a-c). This is consistent with most LPEE age models that reveal early Eocene carbon cycle perturbations close to long eccentricity maxima (Cramer et al., 2003; Zachos et al., 2010). Recent studies also indicate that the PETM appeared close to a long eccentricity maximum (e.g., Zeebe and Lourens, 2019; Piedrahita et al., 2022), which coincides with our orbital tuning. Most LPEE CIEs coincide with marly horizons associated with lysocline shoaling (Fig. 4d; Giusberti et al., 2009; Galeotti et al., 2010). Our $CaCO_3$ record is visually similar to a previous high-resolution $CaCO_3$ record from the Contessa Road section (Galeotti et al., 2010) for which the lowest $CaCO_3$ contents are above ~30-40% (Fig. 4d). This confirms that Contessa Road was less affected by $CaCO_3$ dissolution than other locations, where CIEs are related to sediments with $CaCO_3$ contents below ~5%-e.g., Sites 1262 and 1263 from ODP Leg 208 (Zachos et al., 2005).

CIEs for globally recognized paired events such as ETM 2/H2 and I1/I2 coincide with ascending flanks of successive short eccentricity cycles (Fig. 4a-c). At Contessa Road, the PETM follows a similar pattern with two CIEs that appear in consecutive ascending flanks of short eccentricity cycles (Fig. 4a-c). PETM CIEs are related to marly horizons separated by a $CaCO_3$-rich interval (Figs. 1b-d, 4c-d). These patterns are also identified in the carbon cycle perturbations that appear ~400 kyr after the ETM 3 hyperthermal, which had been recognized as the L event (e.g., Lauretano et al., 2018). We identify here a paired L1/L2 carbon cycle perturbation with a double spike in the Contessa Road δ^{13}C record (Fig. 4c).

Our tuning-based Contessa Road age model indicates a ~350 kyr gap between outcrops A and B (Fig. 4). Discontinuous tuning
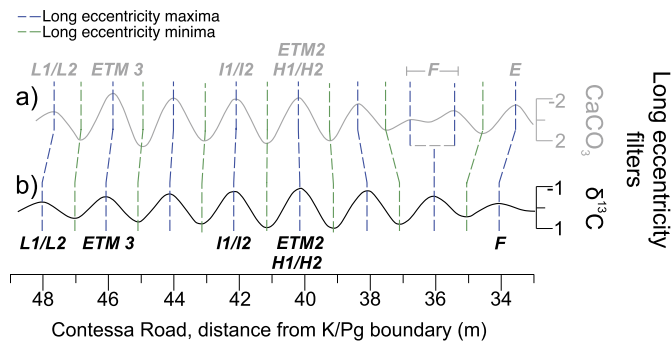
Fig. 5. Contessa Road $CaCO_3$-based (grey line, Galeotti et al., 2010) and δ^{13}C-based (black line) cyclostratigraphic frameworks for Contessa Road outcrop B. Long eccentricity cycles of δ^{13}C are presented in terms of mean from the probabilistic-based age model of outcrop B. CIEs are indicated in grey for filtered long eccentricity cycles of the $CaCO_3$ record of Galeotti et al. (2010), and in black for the filtered long eccentricity cycles of the δ^{13}C record of this study.

of filtered short eccentricity cycles at the end of outcrop A (interval 32.33-33.00 m; Fig. 3a), interrupted sedimentation across the age interval of the gap, and/or a depth mismatch between these two outcrops may explain the duration of the gap. An alternative $CaCO_3$-based cyclostratigraphic framework from Contessa Road was used to indicate the so-called E event in outcrop B (Fig. 5a; Cramer et al., 2003; Galeotti et al., 2010). This small carbon cycle perturbation has been interpreted to occur four long eccentricity cycles before ETM 2 (Zachos et al., 2010). The ETM 2 hyperthermal is identified at Contessa Road at ~40 m depth, and the E event is assigned at ~34 m from long eccentricity cycles in the $CaCO_3$ record of Galeotti et al. (2010) (Fig. 5a). However, filtered long eccentricity cycles are poorly developed in the 35-37 m interval of that $CaCO_3$ record (Fig. 5a), which contains several periods with marked $CaCO_3$ reductions that do not correlate well with CIE events (Fig. 4d). This pattern may reflect $CaCO_3$ dissolution by non-orbitally controlled processes (Fig. 5a). Our probabilistic-based cyclostratigraphic framework reveals only three long eccentricity cycles in the ~34-40 m interval at Contessa Road (Fig. 5b). Well-developed long eccentricity cycles across this interval indicate that the E event did not occur at ~34 m at Contessa Road. In contrast, the long eccentricity maximum at ~34 m is associated here with the F event (Fig. 5b; Cramer et al., 2003). This difference represents the only major variation between our updated chronology and previous age models for Contessa Road (Fig. 5). The events identified in our paleoclimatic interpretations (PETM, ETM 2, H2, I1, ETM 3, and L1) coincide in depth with the $CaCO_3$-based cyclostratigraphic framework of Galeotti et al. (2010). Some age differences between the $CaCO_3$-based astrochronological age model of Galeotti et al. (2010) and our δ^{13}C-based chronology may be related to the astronomical solution used in each study.

3.3. Exponential δ^{13}C recovery

We fit exponential decay functions through the CIE recovery intervals of the PETM, ETM 2, H2, and I1 events at both Contessa Road and ODP Site 1262 (Fig. 6; Table S1). Further CIE recovery exponential decay functions for ETM 3 and L1 were produced only for Contessa Road. Events F, I2, and L2 were excluded here due to their poorly defined CIEs in the Contessa Road δ^{13}C record (Fig. 4c-d). We use our own δ^{13}C data and tuning-based age model for Contessa Road, and independent δ^{13}C data and precession-based age models for ODP Site 1262 (Zachos et al., 2005; Westerhold et al., 2007; Littler et al., 2014). Orbital tuning to astronomical solutions and precession cycle counting are used widely to generate reliable age models (e.g., Westerhold et al., 2007; Littler et al., 2014; Zeebe and Lourens, 2019). These approaches produce differ-

ent floating chronologies, which ensures that our interpretations do not depend exclusively on a single age model or on the absolute age of LPEE CIEs.

At Contessa Road, the initial PETM CIE peak is followed by an immediate transition to heavier δ^{13}C values. An exponential decay function can be fitted roughly following the PETM CIE peak (Fig. 6a, grey; Table S1) with $t_{1/2} = 138^{+24}/_{-19}$ kyr (95% confidence interval). However, a second smaller CIE ~85 kyr after the PETM onset (Fig. 4c, 6a) disrupts the trend to more positive values after the initial PETM CIE peak. This suggests that different exponential decay functions can provide better assessment of the Contessa Road PETM δ^{13}C record. The initial CIE peak was fitted to an exponential decay function with $t_{1/2} = 18^{+26}/_{-8}$ kyr (Fig. 6a, blue; Table S1), while the second PETM CIE has $t_{1/2} = 26^{+5}/_{-3}$ kyr (Fig. 6a, magenta; Table S1). The ODP Site 1262 PETM δ^{13}C record does not have two clear CIEs (Zachos et al., 2005). The PETM recovery there is indicated by a single exponential fit with $t_{1/2} = 13^{+3}/_{-2}$ kyr (Fig. 6b; Table S1). The $t_{1/2}$ values for fits through the δ^{13}C recovery intervals of ETM 2, H2, and I1 at Contessa Road and ODP Site 1262 range from $6^{+6}/_{-4}$ kyr to $14^{+16}/_{-9}$ kyr (Fig. 6c-h), while $t_{1/2}$ for ETM 3 and L1 at Contessa Road are $6^{+2}/_{-2}$ kyr and $16.6^{+31}/_{-10}$ kyr, respectively (Fig. 6i-j).

4. Discussion

4.1. Paleocene-Eocene orbital cycles and PETM light carbon releases

Orbital forcing of the early Eocene carbon cycle has been inferred from several δ^{13}C records (Cramer et al., 2003; Littler et al., 2014; Zeebe et al., 2017). This process has been associated with light carbon releases triggered by thermal destabilization of carbon reservoirs during long and short eccentricity maxima (Lunt et al., 2011; DeConto et al., 2012). Light carbon releases are reflected in more negative δ^{13}C values, which confirms that orbital signals of δ^{13}C records have contrasting patterns with respect to astronomical solutions–i.e., eccentricity maxima coincide with more negative δ^{13}C values (Fig. 5b-c; Zeebe et al., 2017). Early Eocene long and short eccentricity cycles in the Contessa Road δ^{13}C record reveal that this section also contains evidence of orbital controls on the carbon cycle.

Orbitally controlled LPEE carbon cycle conditions promoted $CaCO_3$ dissolution associated with lysocline shoaling and ocean acidification (Galeotti et al., 2010; Zachos et al., 2010). Lysocline depth variations generally produced partial $CaCO_3$ dissolution, as indicated by slight detrital element concentration increases and small $CaCO_3$ reductions in diverse marine sedimentary sections (Westerhold et al., 2007; Zachos et al., 2010; Francescone et al., 2019). In contrast, major ocean acidification events are related to marked detrital element concentration increases that correlate with significant $CaCO_3$ reductions (Westerhold et al., 2007; Zachos et al., 2010; Francescone et al., 2019). These sedimentation patterns have been identified previously at Contessa Road outcrop A (Piedrahita et al., 2022), and are confirmed here by short eccentricity cycles of the χ record (Fig. 4b).

Orbitally controlled $CaCO_3$ dissolution cycles are not recorded in numerous PETM sections. PETM sedimentation is generally characterized by sustained $CaCO_3$ dissolution and low-δ^{13}C values (Fig. 7a-f; Bains et al., 1999; Zachos et al., 2005; Zeebe et al., 2009; Bowen, 2013; Kelly et al., 2012; Bowen et al., 2015; Frieling et al., 2016). Several PETM δ^{13}C records with protracted CIEs contain weak evidence of a second CIE (Fig. 7a-f). We find that the Western Tethyan Contessa Road, Forada (Tipple et al., 2011), and Zumaia (Dunkley Jones et al., 2018) sections record a well-developed second CIE (Fig. 7g-i). This second CIE is also identified at ODP Site 1267; however, evidence of sustained low-δ^{13}C and low-$CaCO_3$ values at adjacent South Atlantic ODP Sites 1262, 1263,
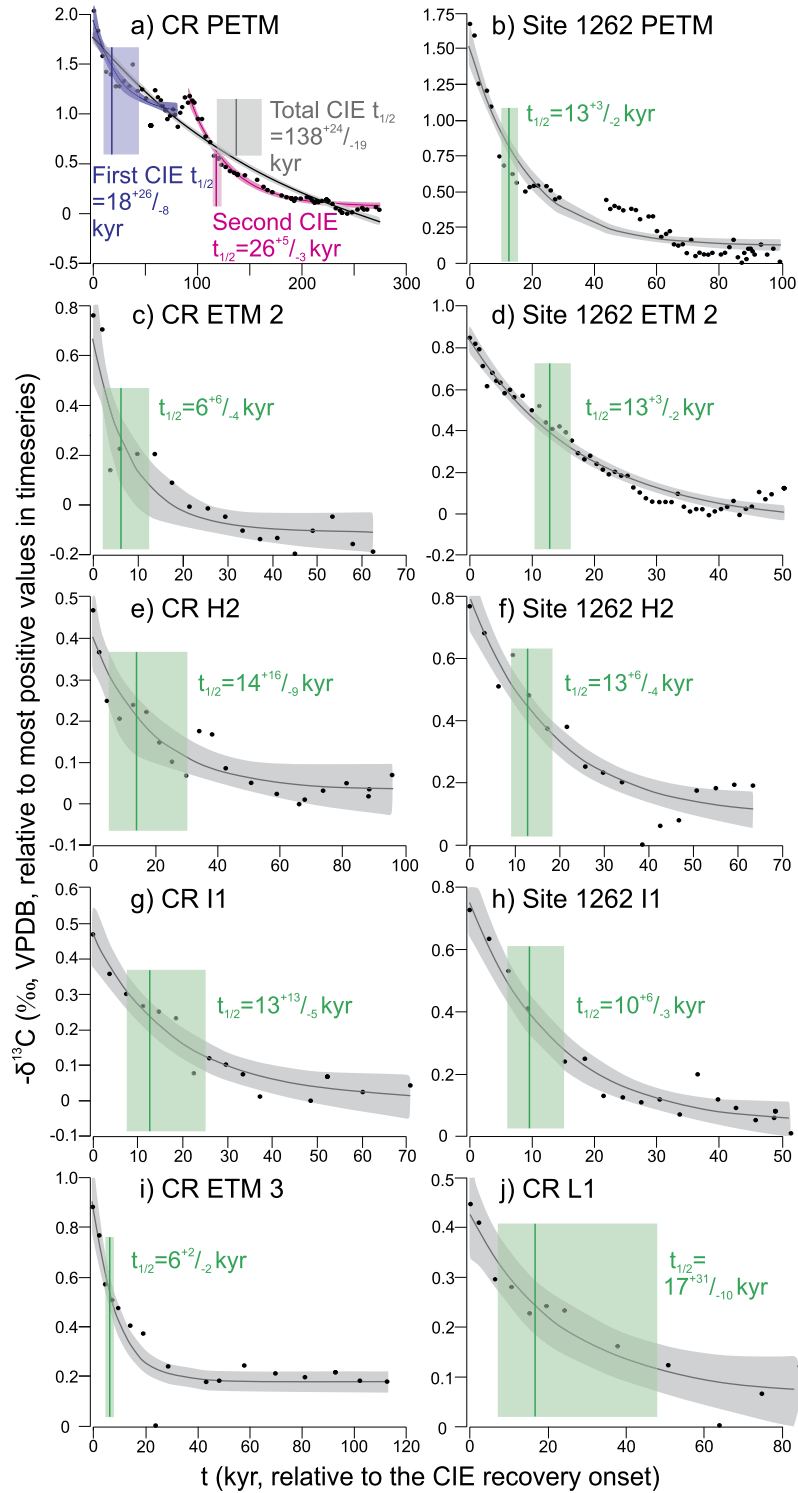
Fig. 6. (a) Contessa Road PETM exponential decay function. The δ^{13}C data are not well fitted by a single exponential decay function (grey tones). A more appropriate fit is obtained by treating two carbon pulses separately with an initial (blue tones) and a second carbon recovery (fuchsia tones). $t_{1/2}$ estimates for each exponential function are indicated by coloured bands. Green bands are used to represent $t_{1/2}$ estimates of exponential decay functions for (b) ODP Site 1262 PETM, (c) Contessa Road ETM 2, (d) ODP Site 1262 ETM 2, (e) Contessa Road H2, (f) ODP Site 1262 H2, (g) Contessa Road I1, (h) ODP Site 1262 I1, (i) Contessa Road ETM 3, and (j) Contessa Road L1. All probabilistic assessments are presented in terms of median (darker tones) and 95% confidence interval (lighter tones).
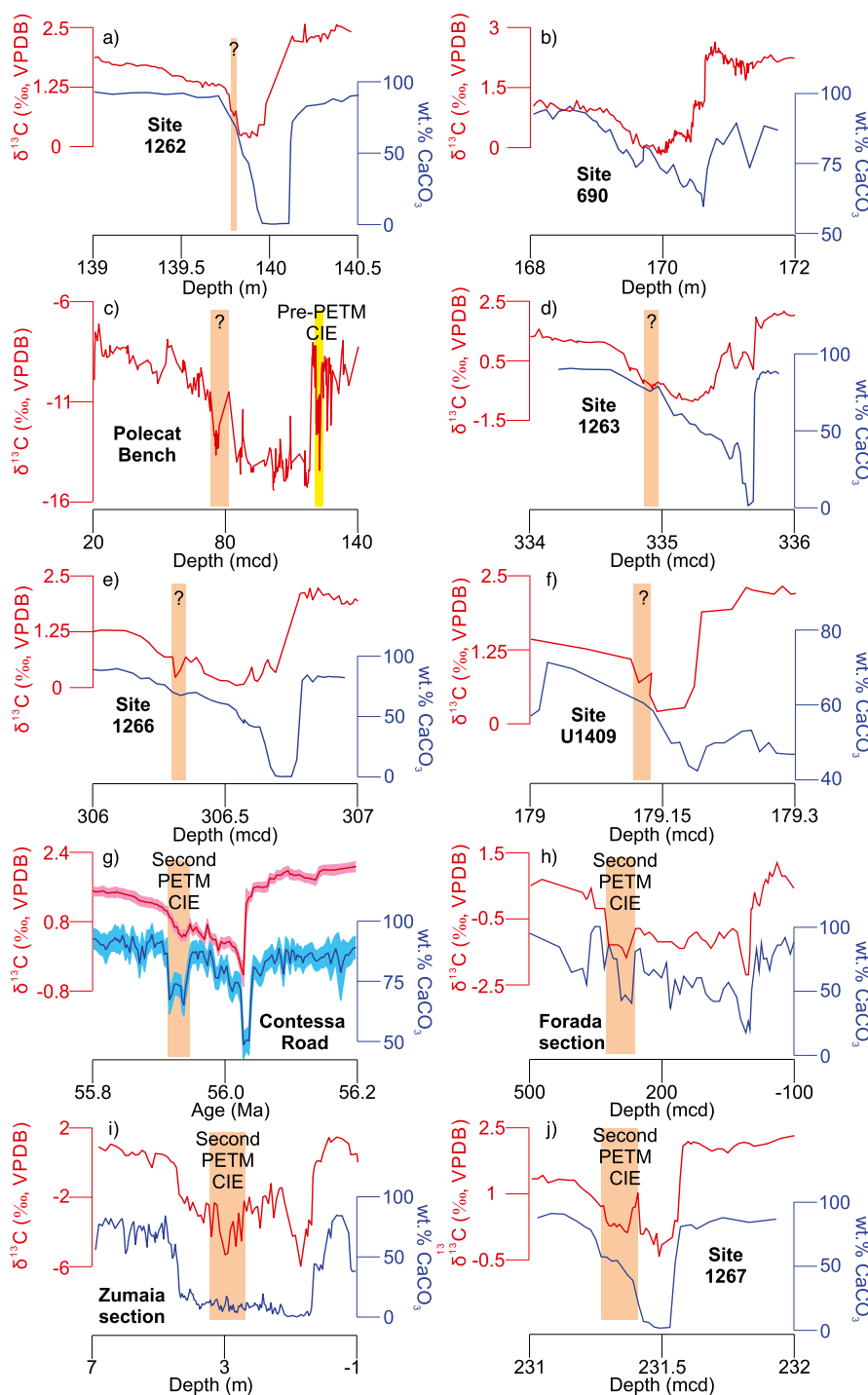
Fig. 7. PETM δ^{13}C (red tones) and CaCO$_3$ (blue tones) records. (a) South Atlantic ODP Site 1262 (Zachos et al., 2005). (b) Southern Ocean ODP Site 690 (Bains et al., 1999; Kelly et al., 2012). (c) North American terrestrial Polecat Bench (Bowen et al., 2015). (d) South Atlantic ODP Site 1263 (Zachos et al., 2005). (e) South Atlantic ODP Site 1266 (Zachos et al., 2005). (f) North Atlantic IODP Site U1409 (Penman et al., 2016). (g) Western Tethyan Contessa Road. (h) Forada section (Tipple et al., 2011). (i) Zumaia section (Dunkley Jones et al., 2018). (j) South Atlantic ODP Site 1267 (Zachos et al., 2005). CR δ^{13}C and CaCO$_3$ records are presented with mean and 2SE. Second PETM CIE events are indicated by orange bands. Question marks in (a), (c), (d), (e), and (f) indicate weak development of this feature. The yellow bar in (c) represents a pre-PETM CIE (Bowen et al., 2015).

and 1266 (Fig. 7a, d, e) may indicate that the PETM record at ODP Site 1267 was affected by bioturbation (e.g., Hupp and Kelly, 2020).

Western Tethyan sections have contrasting sedimentation patterns despite being deposited at similar paleo-water depths (600-1500 m; Giusberti et al., 2009; Galeotti et al., 2010; Tipple et al., 2011; Dunkley Jones et al., 2018). The Zumaia section has sustained low-$CaCO_3$ after the PETM (Fig. 7i), which has been associated with terrigenous inputs and $CaCO_3$ dilution (Dunkley Jones et al., 2018). Alternatively, Contessa Road and Forada have two well-defined $CaCO_3$ reductions that coincide with the two PETM CIEs (Fig. 7g-h). Sedimentation patterns at Forada may have been influenced by both $CaCO_3$ dissolution and dilution (Tipple et al., 2011; Dunkley Jones et al., 2018); therefore, a clear relationship between the second CIE and its associated $CaCO_3$ content reduction cannot be attributed to a single process. In contrast, PETM $CaCO_3$ dissolution horizons at Contessa Road are interpreted to be exclusively associated with lysocline shoaling because minimal terrigenous sedimentation is recorded there (Giusberti et al., 2009; Coccioni et al., 2019). Considering the common LPEE ocean acidification controls on lysocline depth variations (e.g., Zachos et al., 2005), the second PETM marly horizon at Contessa Road can be interpreted as a marker of a second ocean acidification event that affected the western Tethys Ocean.

The PETM interval at Contessa Road contains orbital signals that reflect the occurrence of CIEs and $CaCO_3$ dissolution during short eccentricity maxima, while the limestone layer that separates these marls was deposited during short eccentricity minima (Fig. 4b-c). These PETM $\delta^{13}C/CaCO_3$ patterns are similar to those for other globally recognized early Eocene paired carbon release events (Cramer et al., 2003; Galeotti et al., 2010; Zachos et al., 2010). Triggering of early Eocene carbon cycle perturbations has been associated with high seasonal contrast of both long and short eccentricity maxima. Enhanced expression of short eccentricity cycles across long eccentricity maxima produced paired CIEs (Cramer et al., 2003; Zachos et al., 2010; Lunt et al., 2011; DeConto et al., 2012; Barnet et al., 2019). This mechanism may explain CIE patterns across western Tethyan sections, and suggests that Contessa Road contains evidence of a second, orbitally controlled, light carbon injection. This interpretation is confirmed by PETM foraminiferal assemblages. Foraminiferal assemblages at Contessa Road reveal that the PETM onset coincided with a benthic foraminiferal extinction event. This event was followed by gradual recovery of benthic faunas and $CaCO_3$-rich sedimentation; however, this recovery period was interrupted in the second PETM marly horizon, which records similar foraminiferal assemblages to those identified at the PETM onset (Giusberti et al., 2009). This pattern indicates that benthic foraminiferal changes in both PETM marly layers responded to the same drivers, which also provides evidence that the second PETM CIE corresponds to a second light carbon injection. Orbital signals identified at Contessa Road suggest that orbital forcing may have played an important role in CIE triggering of both initial and secondary PETM light carbon injections (Piedrahita et al., 2022). However, this process does not exclude the possibility that the long PETM duration was also associated with volcanic-related carbon emissions (Frieling et al., 2016; Kender et al., 2021).

A second PETM light carbon injection supports the notion that there may have been several discrete PETM light carbon releases. For example, a pre-PETM CIE in North American terrestrial sediments has been used to suggest that repeated light carbon injections occurred across the Paleocene/Eocene boundary (Fig. 7c; Bowen et al., 2015). Volcanic-related carbon emissions, and/or thermal destabilization of carbon reservoirs may have caused sustained low-CIE conditions in several PETM sections after the event onset (Zeebe et al., 2009; Bowen, 2013; Zeebe, 2013; Frieling et al., 2016). Orbitally forced thermal destabilization of organic carbon

reservoirs and/or methane hydrates may have produced a second CIE during the PETM, as is also observed in some later early Eocene hyperthemals (Lunt et al., 2011; DeConto et al., 2012). Diverse $\delta^{13}C$ patterns among PETM sections indicate regionally variable $\delta^{13}C$ local responses to light carbon injections (Fig. 7), which reveals that the influence of secondary PETM carbon releases was not global. This effect may be related to smaller secondary PETM light carbon releases, such as the second orbitally controlled carbon release represented by a small CIE in the Contessa Road $\delta^{13}C$ record. Alternatively, the carbon source origin and location, and/or changing ocean circulation patterns may have limited the light carbon distribution across oceanic basins (Dickens, 2000; Zeebe et al., 2009; Bowen et al., 2015).

4.2. Light carbon sequestration and ocean acidification recovery

$\delta^{13}C$ recovery $t_{1/2}$ estimates of LPEE carbon cycle perturbations at Contessa Road and at ODP Site 1262 are similar to published $t_{1/2}$ values for Southern Ocean and North American PETM records (Fig. 8; Bowen and Zachos, 2010). These values contrast with typical background $t_{1/2}$ estimates for the modern Earth-surface carbon cycle (>100 kyr; Bowen and Zachos, 2010), and confirm the existence of significant differences between the LPEE and the modern carbon cycle (Bowen and Zachos, 2010). LPEE CIEs had markedly different injected carbon masses (e.g., emissions are estimated at 2,000-20,000 Pg for the PETM and 2,600-3,800 Pg for ETM 2; McInerney and Wing, 2011; Gutjahr et al., 2017; Harper et al., 2020). These CIEs were triggered under similar topographic, paleogeographic, and climatic conditions that are verified by overlapping climate sensitivity estimates for diverse LPEE age intervals (McInerney and Wing, 2011; Inglis et al., 2020). Therefore, $t_{1/2}$ estimates for different LPEE CIEs may represent similar carbon sequestration mechanisms. Higher $t_{1/2}$ values are expected for larger events if carbon flux rates remain constant (Bowen and Zachos, 2010); however, LPEE CIEs have similar $t_{1/2}$ estimates for light carbon injections with contrasting magnitudes. This reveals that small $t_{1/2}$ recovery estimates mainly depended on accelerated carbon flux rates associated with enhanced light carbon sequestration (Bowen and Zachos, 2010; Komar and Zeebe, 2017).

For well-defined events at Contessa Road and ODP Site 1262, abrupt $CaCO_3$ increases and Fe reductions coincided temporally with one estimated $t_{1/2}$ period (Fig. 9). These $CaCO_3$/Fe variations indicate ocean acidification recovery and lysocline deepening; therefore, a strong relationship between carbon sequestration and lysocline depth adjustments can be inferred. Lysocline deepening and ocean acidification recovery are consequences of accelerated chemical weathering produced by intensified hydrological cycle conditions under global warming (Hönisch et al., 2012; Penman et al., 2016; Pogge von Strandmann et al., 2021). Chemical weathering causes long-term carbon sequestration, and increases alkalinity and dissolved inorganic carbon delivery to the oceans. These processes eventually increase seawater carbonate saturation, which is reduced dramatically during ocean acidification (Hönisch et al., 2012; Penman et al., 2016; Kitch et al., 2021). High dissolved cation supplies promote $CaCO_3$ production and burial, which drive lysocline depth variations and balance ocean alkalinity (Hönisch et al., 2012; Penman et al., 2016; Komar and Zeebe, 2017). Lysocline deepening at Contessa Road and ODP Site 1262 during CIE recovery reveal enhanced chemical weathering. Chemical weathering feedbacks should have been large enough to reestablish ocean chemistry at sites with different paleogeographic positions and paleo-water depths. Considering that LPEE CIE recovery coincided globally with lysocline deepening (e.g., Littler et al., 2014; Penman et al., 2016; Barnet et al., 2019), ocean circulation may have played a critical role in the dissolved cation distribution and alkalinity reestablishment across different ocean basins. Chemical weathering
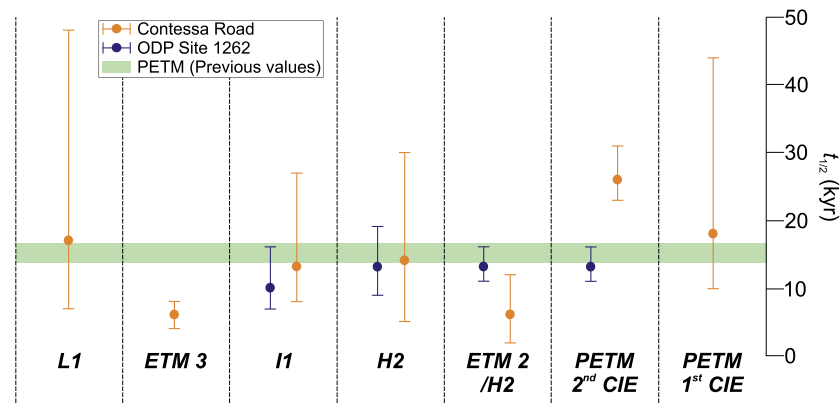
Fig. 8. Contessa Road and ODP Site 1262 $t_{1/2}$ estimates for LPEE carbon cycle perturbations. These values are presented in terms of median and 95% confidence interval. The green bar represents the range of $t_{1/2}$ values obtained for Southern Ocean and North American PETM records (Bowen and Zachos, 2010).
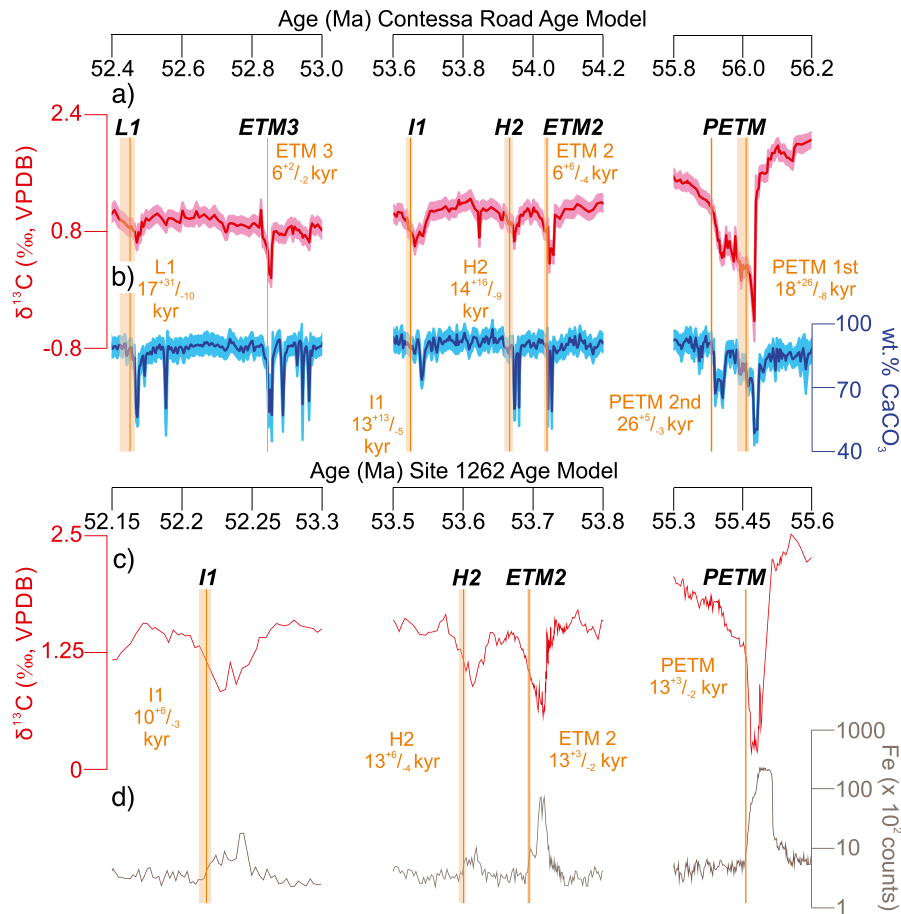

Fig. 9. Contessa Road (a) δ^{13}C and (b) CaCO$_3$ records of LPEE carbon cycle perturbations. ODP Site 1262 (c) δ^{13}C and (d) Fe records of LPEE carbon cycle perturbations (Zachos et al., 2005; Westerhold et al., 2007; Zachos et al., 2010; Littler et al., 2014). $t_{1/2}$ estimates (orange bands) for each event at both sites are expressed in terms of median and 95% confidence interval. These coincide with times over which CaCO$_3$ contents increase at Contessa Road and Fe values decrease at ODP Site 1262. Contessa Road δ^{13}C and CaCO$_3$ records are presented in terms of mean and standard error (SE).

may also have been important in reestablishing the Earth-surface carbon cycle during LPEE CIE recovery; however, chemical weathering timescales can be an order of magnitude larger than $t_{1/2}$ estimates for LPEE carbon cycle perturbations (Bowen and Zachos, 2010). Therefore, carbon removal by other processes is required to produce the relatively short LPEE $t_{1/2}$ values (Bowen and Zachos, 2010). Marine tephra diagenesis has been interpreted to promote CaCO$_3$ cement precipitation within NAIP tephra layers. This process has been suggested to have removed a quarter of released PETM light carbon from the ocean-atmosphere (Longman et al., 2021) and may explain small PETM $t_{1/2}$ values; however, marine tephra diagenesis controls on carbon sequestration of succeeding LPEE carbon cycle perturbations is unclear. Although NAIP activity has been documented following the PETM, early Eocene light carbon injections may have not been triggered by NAIP eruptions. Consequently, negative carbon cycle feedbacks associated with marine tephra diagenesis may have not played a significant role in carbon removal of early Eocene carbon cycle perturbations.

Overlapping $t_{1/2}$ estimates for different LPEE carbon cycle perturbations (Fig. 8) reveal that light carbon removal was optimized to the conditions induced by the initial perturbation. Enhanced chemical weathering during LPEE CIE recovery may have increased ocean nutrient availability, which is compatible with carbon uptake through a redox-controlled carbon-phosphorus feedback identified for the PETM recovery (Komar and Zeebe, 2017). This mechanism is partially regulated by temperature increases that control oxygen solubility and reduce seawater oxygen levels (Weiss, 1970). Similar climate sensitivity estimates for different LPEE age intervals (Inglis et al., 2020) indicate that larger light carbon injections produced higher temperatures (Littler et al., 2014). Therefore, oxygen solubility in seawater, and associated oxygen levels, may have changed according to the size of the initial light carbon release. LPEE light carbon injections should have decreased organic matter remineralization and increased organic matter preservation/burial, due to the induced temperature influence on oxygen levels (Komar and Zeebe, 2017). This process may have modified carbon sequestration rates for each LPEE carbon cycle perturbation, which can explain the small and overlapping $t_{1/2}$ estimates for LPEE CIE recovery. This suggests that the temporal relationship between $t_{1/2}$ estimates and ocean acidification recovery also depended on marine carbon sequestration (Ma et al., 2014; Komar and Zeebe, 2017). Additional carbon removal by growth of terrestrial biosphere stocks and/or shifts in calcification style following LPEE light carbon injections may have also been possible (Bowen and Zachos, 2010; Boudreau et al., 2018). However, our data are insufficient to corroborate these mechanisms.

There are slight variations between Contessa Road and ODP 1262 $t_{1/2}$ estimates (Fig. 8). These may be related to age model differences and/or biological/sedimentary effects on δ^{13}C recording (Bowen, 2013; Hupp and Kelly, 2020). Possible disturbances induced by these factors did not affect greatly our $t_{1/2}$ estimates, which are validated by their similarities to values from other localities (Fig. 8; Bowen and Zachos, 2010). $t_{1/2}$ estimates at both sites reveal that LPEE carbon sequestration was accelerated in response to light carbon injections; however, carbon sequestration appears to have remained slow enough that $t_{1/2}$ estimates ranged from $6^{+2}/_{-2}$ kyr to $26^{+2}/_{-2}$ kyr. These $t_{1/2}$ estimates imply that carbon sequestration feedbacks cannot be accelerated endlessly, and that SSP 8.5-like temperatures and CO$_2$ concentrations may induce negative environmental impacts for thousands of years (Burke et al., 2018; Meinshausen et al., 2020; Rae et al., 2021).

5. Conclusions

LPEE carbon cycle perturbations were associated with light carbon injections that produced ocean acidification and CaCO$_3$ disso-

lution horizons. δ^{13}C and sedimentation patterns at Contessa Road indicate a second PETM CIE that is a result of a second orbitally controlled light carbon injection following the PETM onset. Contrasting δ^{13}C records of western Tethyan sections with respect to those from other locations indicate that secondary PETM light carbon injections did not have global impacts.

LPEE light carbon injections were followed by periods of accelerated carbon sequestration. Similar CIE recovery estimates between LPEE carbon cycle perturbations suggest that light carbon sequestration was accelerated in proportion to the magnitude of initial carbon release. Temperature controls on oxygen solubility may have optimized the biological pump in proportion to the mass of each light carbon injection. This process would have modified productivity feedbacks and shifted carbon sequestration rates.

CRediT authorship contribution statement

Victor A. Piedrahita: Conceptualization, Formal analysis, Methodology, Writing – original draft. **Xiang Zhao:** Software. **Andrew P. Roberts:** Supervision, Writing – review & editing. **Eelco J. Rohling:** Supervision, Writing – review & editing. **David Heslop:** Supervision, Writing – review & editing. **Simone Galeotti:** Supervision, Writing – review & editing. **Laura Rodríguez-Sanz:** Resources, Writing – review & editing. **Fabio Florindo:** Supervision, Writing – review & editing. **Katharine M. Grant:** Resources, Writing – review & editing.

Declaration of competing interest

The authors declare that they have no known competing financial interests or personal relationships that could have appeared to influence the work reported in this paper.

Data availability

Data can be found in the online version of this paper and code is available via FigShare (https://doi.org/10.6084/m9.figshare.21741722.v1).

Acknowledgements

Appendix A. Supplementary material

Supplementary material related to this article can be found online at https://doi.org/10.1016/j.epsl.2023.117992.

References

Bains, S., Corfield, R.M., Norris, R.D., 1999. Mechanisms of climate warming at the end of the Paleocene. Science 285, 724–727. https://doi.org/10.1126/science.285.5428.724.

Barnet, J.S.K., Littler, K., Westerhold, T., Kroon, D., Leng, M.J., Bailey, I., Röhl, U., Zachos, J.C., 2019. A high-fidelity benthic stable isotope record of late Cretaceous-early Eocene climate change and carbon-cycling. Paleoceanogr. Paleoclimatol. 34, 672–691. https://doi.org/10.1029/2019PA003556.

Bowen, G.J., Zachos, J.C., 2010. Rapid carbon sequestration at the termination of the Palaeocene-Eocene Thermal Maximum. Nat. Geosci. 3, 866–869. https://doi.org/10.1038/ngeo1014.

Bowen, G.J., 2013. Up in smoke: a role for organic carbon feedbacks in Paleogene hyperthermals. Glob. Planet. Change 109, 18–29. https://doi.org/10.1016/j.gloplacha.2013.07.001.

Bowen, G.J., Maibauer, B.J., Kraus, M.J., Röhl, U., Westerhold, T., Steimke, A., Gingerich, P.D., Wing, S.L., Clyde, W.C., 2015. Two massive, rapid releases of carbon during the onset of the Palaeocene-Eocene thermal maximum. Nat. Geosci. 8, 44–47. https://doi.org/10.1038/ngeo2316.

Boudreau, B.P., Middelburg, J.J., Luo, Y., 2018. The role of calcification in carbonate compensation. Nat. Geosci. 11, 894–900. https://doi.org/10.1038/s41561-018-0259-5.

Burke, K.D., Williams, J.W., Chandler, M.A., Haywood, A.M., Lunt, D.J., Otto-Bliesner, B.L., 2018. Pliocene and Eocene provide best analogs for near-future climates. Proc. Natl. Acad. Sci. USA 115, 13288–13293. https://doi.org/10.1073/pnas.1809600115.

Coccioni, R., Frontalini, F., Catanzariti, R., Jovane, L., Rodelli, D., Rodrigues, I.M., Savian, J.F., Giorgioni, M., Galbrun, B., 2019. Paleoenvironmental signature of the Selandian-Thanetian transition event (STTE) and Early Late Paleocene Event (ELPE) in the Contessa Road section (western Neo-Tethys). Palaeogeogr. Palaeoclimatol. Palaeoecol. 523, 62–77. https://doi.org/10.1016/j.palaeo.2019.03.023.

Cramer, B.S., Wright, J.D., Kent, D.V., Aubry, M.-P., 2003. Orbital climate forcing of δ^{13}C excursions in the late Paleocene-early Eocene (chrons C24n-C25n). Paleoceanography 18, 1097. https://doi.org/10.1029/2003PA000909.

DeConto, R.M., Galeotti, S., Pagani, M., Tracy, D., Schaefer, K., Zhang, T., Pollard, D., Beerling, D.J., 2012. Past extreme warming events linked to massive carbon release from thawing permafrost. Nature 484, 87–91. https://doi.org/10.1038/nature10929.

Dickens, G.R., 2000. Methane oxidation during the late Palaeocene Thermal Maximum. Bull. Soc. Géol. Fr. 171, 37–49.

Dunkley Jones, T., Manners, H.R., Hoggett, M., Kirtland Turner, S., Westerhold, T., Leng, M.J., Pancost, R.D., Ridgwell, A., Alegret, L., Duller, R., Grimes, S.T., 2018. Dynamics of sediment flux to a bathyal continental margin section through the Paleocene-Eocene Thermal Maximum. Clim. Past 14, 1035–1049. https://doi.org/10.5194/cp-14-1035-2018.

Francescone, F., Lauretano, V., Bouligand, C., Moretti, M., Sabatino, N., Schrader, C., Catanzariti, R., Hilgen, F., Lanci, L., Turtù, A., Sprovieri, M., Lourens, L., Galeotti, S., 2019. A 9 million-year-long astrochronological record of the early-middle Eocene corroborated by seafloor spreading rates. Geol. Soc. Am. Bull. 131, 499–520. https://doi.org/10.1130/B32050.1.

Frieling, J., Svensen, H.H., Planke, S., Cramwinckel, M.J., Selnes, H., Sluijs, A., 2016. Thermogenic methane release as a cause for the long duration of the PETM. Proc. Natl. Acad. Sci. USA 113, 12059–12064. https://doi.org/10.1073/pnas.1603348113.

Galeotti, S., Krishnan, S., Pagani, M., Lanci, L., Gaudio, A., Zachos, J.C., Monechi, S., Morelli, G., Lourens, L., 2010. Orbital chronology of early Eocene hyperthermals from the Contessa Road section, central Italy. Earth Planet. Sci. Lett. 290, 192–200. https://doi.org/10.1016/j.epsl.2009.12.021.

Giusberti, L., Coccioni, R., Sprovieri, M., Tateo, F., 2009. Perturbation at the sea floor during the Paleocene-Eocene Thermal Maximum: evidence from benthic foraminifera at Contessa Road, Italy. Mar. Micropaleontol. 70, 102–119. https://doi.org/10.1016/j.marmicro.2008.11.003.

Gutjahr, M., Ridgwell, A., Sexton, P.F., Anagnostou, E., Pearson, P.N., Pälike, H., Norris, R.D., Thomas, E., Foster, G.L., 2017. Very large release of mostly volcanic carbon during the Paleocene-Eocene Thermal Maximum. Nature 548, 573–577. https://doi.org/10.1038/nature23646.

Harper, D.T., Hönisch, B., Zeebe, R.E., Shaffer, G., Haynes, L.L., Thomas, E., Zachos, J.C., 2020. The magnitude of surface ocean acidification and carbon release during Eocene Thermal Maximum 2 (ETM-2) and the Paleocene-Eocene Thermal Maximum (PETM). Paleoceanogr. Paleoclimatol. 35, e2019PA003699. https://doi.org/10.1029/2019PA003699.

Hönisch, B., Ridgwell, A., Schmidt, D.N., Thomas, E., Gibbs, S.J., Sluijs, A., Zeebe, R.E., Kump, L., Martindale, R.C., Greene, S.E., Kiessling, W., Ries, J., Zachos, J.C., Royer, D.L., Barker, S., Marchitto Jr, T.M., Moyer, R., Pelejero, C., Ziveri, P., Foster, G.L., Williams, B., 2012. The geological record of ocean acidification. Science 335, 1058–1063. https://doi.org/10.1126/science.1208277.

Hupp, B., Kelly, D.C., 2020. Delays, discrepancies, and distortions: size-dependent sediment mixing and the deep-sea record of the Paleocene-Eocene Thermal Maximum from ODP Site 690 (Weddell Sea). Paleoceanogr. Paleoclimatol. 35, e2020PA004018. https://doi.org/10.1029/2020PA004018.

Inglis, G.N., Bragg, F., Burls, N.J., Cramwinckel, M.J., Evans, D., Foster, G.L., Huber, M., Lunt, D.J., Siler, N., Steinig, S., Tierney, J.E., Wilkinson, R., Anagnostou, E., de Boer, A.M., Dunkley Jones, T., Edgar, K.M., Hollis, C.J., Hutchinson, D.K., Pancost, R.D., 2020. Global mean surface temperature and climate sensitivity of the early Eocene Climatic Optimum (EECO), Paleocene-Eocene Thermal Maximum (PETM), and latest Paleocene. Clim. Past 16, 1953–1968. https://doi.org/10.5194/cp-16-1953-2020.

Kelly, D.C., Nielsen, T.M., Schellenberg, S.A., 2012. Carbonate saturation dynamics during the Paleocene-Eocene Thermal Maximum: bathyal constraints from ODP sites 689 and 690 in the Weddell Sea (South Atlantic). Mar. Geol. 303, 75–86. https://doi.org/10.1016/j.margeo.2012.02.003.

Kender, S., Bogus, K., Pedersen, G.K., Dybkjær, K., Mather, T.A., Mariani, E., Ridgwell, A., Riding, J.B., Wagner, T., Hesselbo, S.P., Leng, M.J., 2021. Paleocene/Eocene carbon feedbacks triggered by volcanic activity. Nat. Commun. 12, 1–10. https://doi.org/10.1038/s41467-021-25536-0.

Kitch, G.D., Jacobson, A.D., Harper, D.T., Hurtgen, M.T., Sageman, B.B., Zachos, J.C., 2021. Calcium isotope composition of Morozovella over the late Paleocene-early Eocene. Geology 49, 723–727. https://doi.org/10.1130/G48619.1.

Komar, N., Zeebe, R.E., 2017. Redox-controlled carbon and phosphorus burial: a mechanism for enhanced organic carbon sequestration during the PETM. Earth Planet. Sci. Lett. 479, 71–82. https://doi.org/10.1016/j.epsl.2017.09.011.

Lauretano, V., Zachos, J.C., Lourens, L.J., 2018. Orbitally paced carbon and deep-sea temperature changes at the peak of the early Eocene climatic optimum. Paleoceanogr. Paleoclimatol. 32, 1050–1065. https://doi.org/10.1029/2018PA003422.

Littler, K., Röhl, U., Westerhold, T., Zachos, J.C., 2014. A high-resolution benthic stable-isotope record for the South Atlantic: implications for orbital-scale changes in late Paleocene-early Eocene climate and carbon cycling. Earth Planet. Sci. Lett. 401, 18–30. https://doi.org/10.1016/j.epsl.2014.05.054.

Longman, J., Gernon, T.M., Palmer, M.R., Jones, M.T., Stokke, E.W., Svensen, H.H., 2021. Marine diagenesis of tephra aided the Palaeocene-Eocene Thermal Maximum termination. Earth Planet. Sci. Lett. 571, 117101. https://doi.org/10.1016/j.epsl.2021.117101.

Lourens, L.J., Sluijs, A., Kroon, D., Zachos, J.C., Thomas, E., Röhl, U., Bowles, J., Raffi, I., 2005. Astronomical pacing of late Palaeocene to early Eocene global warming events. Nature 435, 1083–1087. https://doi.org/10.1038/nature03814.

Lunt, D.J., Ridgwell, A., Sluijs, A., Zachos, J., Hunter, S., Haywood, A., 2011. A model for orbital pacing of methane hydrate destabilization during the Palaeogene. Nat. Geosci. 4, 775–778. https://doi.org/10.1038/ngeo1266.

Ma, Z., Gray, E., Thomas, E., Murphy, B., Zachos, J.C., Paytan, A., 2014. Carbon sequestration during the Palaeocene-Eocene Thermal Maximum by an efficient biological pump. Nat. Geosci. 7, 382–388. https://doi.org/10.1038/ngeo2139.

McInerney, F.A., Wing, S.L., 2011. The Paleocene-Eocene Thermal Maximum: a perturbation of carbon cycle, climate, and biosphere with implications for the future. Annu. Rev. Earth Planet. Sci. 39, 489–516. https://doi.org/10.1146/annurev-earth-040610-133431.

Meinshausen, M., Nicholls, Z.R.J., Lewis, J., Gidden, M.J., Vogel, E., Freund, M., Beyerle, U., Gessner, C., Nauels, A., Bauer, N., Canadell, J.G., Daniel, J.S., John, A., Krummel, P.B., Luderer, G., Meinshausen, N., Montzka, S.A., Rayner, P.J., Reimann, S., Smith, S.J., van den Berg, M., Velders, G.J.M., Vollmer, M.K., Wang, R.H.J., 2020. The shared socio-economic pathway (SSP) greenhouse gas concentrations and their extensions to 2500. Geosci. Model Dev. 13, 3571–3605. https://doi.org/10.5194/gmd-13-3571-2020.

Penman, D.E., Kirtland Turner, S., Sexton, P.F., Norris, R.D., Dickson, A.J., Boulila, S., Ridgwell, A., Zeebe, R.E., Zachos, J.C., Cameron, A., Westerhold, T., Röhl, U., 2016. An abyssal carbonate compensation depth overshoot in the aftermath of the Palaeocene-Eocene Thermal Maximum. Nat. Geosci. 9, 575–580. https://doi.org/10.1038/ngeo2757.

Piedrahita, V.A., Galeotti, S., Zhao, X., Roberts, A.P., Rohling, E.J., Heslop, D., Florindo, F., Grant, K.M., Rodríguez-Sanz, L., Reghellin, D., Zeebe, R.E., 2022. Orbital phasing of the Paleocene-Eocene Thermal Maximum. Earth Planet. Sci. Lett. 598, 117839. https://doi.org/10.1016/j.epsl.2022.117839.

Pogge von Strandmann, P.A., Jones, M.T., West, A.J., Murphy, M.J., Stokke, E.W., Tarbuck, G., Wilson, D.J., Pearce, C.R., Schmidt, D.N., 2021. Lithium isotope evidence for enhanced weathering and erosion during the Paleocene-Eocene Thermal Maximum. Sci. Adv. 7, eabh4224. https://doi.org/10.1126/sciadv.abh4224.

Rae, J.W., Zhang, Y.G., Liu, X., Foster, G.L., Stoll, H.M., Whiteford, R.D., 2021. Atmospheric CO_2 over the past 66 million years from marine archives. Annu. Rev. Earth Planet. Sci. 49, 609–641. https://doi.org/10.1146/annurev-earth-082420-063026.

Tanaka, E., Yasukawa, K., Ohta, J., Kato, Y., 2022. Enhanced continental chemical weathering during the multiple early Eocene hyperthermals: new constraints from the southern Indian Ocean. Geochim. Cosmochim. Acta 331, 192–211. https://doi.org/10.1016/j.gca.2022.05.022.

Tipple, B.J., Pagani, M., Krishnan, S., Dirghangi, S.S., Galeotti, S., Agnini, C., Giusberti, L., Rio, D., 2011. Coupled high-resolution marine and terrestrial records of carbon and hydrologic cycles variations during the Paleocene–Eocene Thermal Maximum (PETM). Earth Planet. Sci. Lett. 311, 82–92. https://doi.org/10.1016/j.epsl.2011.08.045.

van der Meulen, B., Gingerich, P.D., Lourens, L.J., Meijer, N., van Broekhuizen, S., van Ginneken, S., Abels, H.A., 2020. Carbon isotope and mammal recovery from extreme greenhouse warming at the Paleocene-Eocene boundary in astronomically-calibrated fluvial strata, Bighorn Basin, Wyoming, USA. Earth Planet. Sci. Lett. 534, 116044. https://doi.org/10.1016/j.epsl.2019.116044.

Weiss, R., 1970. The solubility of nitrogen, oxygen and argon in water and seawater. Deep-Sea Res. 17, 721–735. https://doi.org/10.1016/0011-7471(70)90037-9.

Westerhold, T., Röhl, U., Laskar, J., Raffi, I., Bowles, J., Lourens, L.J., Zachos, J.C., 2007. On the duration of magnetochrons C24r and C25n and the timing of early Eocene global warming events: implications from the Ocean Drilling Program Leg 208 Walvis Ridge depth transect. Paleoceanography 22, PA2201. https://doi.org/10.1029/2006PA001322.

Westerhold, T., Marwan, N., Drury, A.J., Liebrand, D., Agnini, C., Anagnostou, E., Barnet, J.S.K., Bohaty, S.M., De Vleeschouwer, D., Florindo, F., Frederichs, T., Hodell, D.A., Holbourn, A.E., Kroon, D., Lauretano, V., Littler, K., Lourens, L.J., Lyle, M., Pälike, H., Röhl, U., Tian, J., Wilkens, R.H., Wilson, P.A., Zachos, J.C., 2020. An astronomically dated record of Earth's climate and its predictability over the last 66 million years. Science 369, 1383–1387. https://doi.org/10.1126/science.aba6853.

Yasukawa, K., Nakamura, K., Fujinaga, K., Ikehara, M., Kato, Y., 2017. Earth system feedback statistically extracted from the Indian Ocean deep-sea sediments recording Eocene hyperthermals. Sci. Rep. 7, 1–12. https://doi.org/10.1038/s41598-017-11470-z.

Zachos, J.C., Röhl, U., Schellenberg, S.A., Sluijs, A., Hodell, D.A., Kelly, D.C., Thomas, E., Nicolo, M., Raffi, I., Lourens, L.J., McCarren, H., Kroon, D., 2005. Rapid acidification of the ocean during the Paleocene-Eocene Thermal Maximum. Science 308, 1611–1615. https://doi.org/10.1126/science.1109004.

Zachos, J.C., McCarren, H., Murphy, B., Röhl, U., Westerhold, T., 2010. Tempo and scale of late Paleocene and early Eocene carbon isotope cycles: implications for the origin of hyperthermals. Earth Planet. Sci. Lett. 299, 242–249. https://doi.org/10.1016/j.epsl.2010.09.004.

Zeebe, R.E., Zachos, J.C., Dickens, G.R., 2009. Carbon dioxide forcing alone insufficient to explain Palaeocene-Eocene Thermal Maximum warming. Nat. Geosci. 2, 576–580. https://doi.org/10.1038/ngeo578.

Zeebe, R.E., 2013. What caused the long duration of the Paleocene-Eocene Thermal Maximum? Paleoceanography 28, 440–452. https://doi.org/10.1002/palo.20039.

Zeebe, R.E., Westerhold, T., Littler, K., Zachos, J.C., 2017. Orbital forcing of the Paleocene and Eocene carbon cycle. Paleoceanography 32, 440–465. https://doi.org/10.1002/2016PA003054.

Zeebe, R.E., Lourens, L.J., 2019. Solar System chaos and the Paleocene-Eocene boundary age constrained by geology and astronomy. Science 365, 926–929. https://doi.org/10.1126/science.aax0612.